

# Nanopillar quantum well lasers directly grown on silicon and emitting at silicon-transparent wavelengths: supplementary material

FANGLU LU,<sup>§,1</sup> INDRASEN BHATTACHARYA,<sup>§,2</sup> HAO SUN,<sup>3</sup> THAI-TRUONG D. TRAN,<sup>2</sup> KAR WEI NG,<sup>1</sup> GILLIARD N. MALHEIROS-SILVEIRA,<sup>1</sup> CONNIE CHANG-HASNAIN<sup>1,2</sup>

<sup>1</sup>Department of Electrical Engineering and Computer Sciences, University of California at Berkeley, Berkeley, California 94720, US

<sup>2</sup>Applied Science and Technology Group, University of California at Berkeley, Berkeley, California 94720, USA

<sup>3</sup>Department of Electronic Engineering, Tsinghua University, Beijing 100084, China

<sup>§</sup>Equal contribution

\*Corresponding author: [cch@berkeley.edu](mailto:cch@berkeley.edu)

Published 23 June 2017

This article provides supplementary information to "Nanopillar quantum well lasers directly grown on silicon and emitting at silicon-transparent wavelengths," <https://doi.org/10.1364/optica.4.000717>. © 2017

Optical Society of America

<https://doi.org/10.1364/optica.4.000717.s001>

## I. FERMI LEVEL SPLIT MEASUREMENT

The quasi Fermi level split  $\Delta F$  of electrons and holes at steady state in a semiconductor is equal to the chemical potential  $\mu$  of emitted photons [1]. The chemical potential of the photons determines the photon population statistics and hence the quantitative photoluminescence (PL) intensity from the nanopillar:

$$r_{sp}(\hbar\omega, \mu) = \frac{2\pi(\hbar\omega)^2}{h^3 c^2} \times \frac{a(\hbar\omega, \Delta F)}{e^{\frac{\hbar\omega - \mu}{k_B T}} - 1} \quad (S1)$$

where  $r_{sp}$  is the energy-resolved photoluminescence intensity in photons/s/cm<sup>2</sup>/eV,  $\hbar\omega$  is the photon energy,  $h$  is Planck's constant,  $c$  is the speed of light,  $k_B$  is the Boltzmann constant,  $T$  is the lattice temperature and  $a(\hbar\omega, \mu)$  is the dimensionless absorptivity (or equivalently emissivity) of the quantum well. The absorptivity depends on the photon energy through the quantum well bandgap and quantization energy, as well as on the chemical potential (= quasi Fermi level split) through the Fermi inversion factor at any given excitation level. From a calculation based on Fermi's golden rule, and verified with transferred 2D membranes of InAs, the absorptivity for photons above the effective bandgap is related to the fine structure constant and surrounding medium's index of refraction ( $n_r$ ) [2]:  $a = \frac{\pi\alpha}{n_r} = 0.7\%$ . This is not very different from the value obtained for a simplistic Beer-Lambert law calculation for an InGaAs double heterostructure with a thickness on the scale of 5-10 nm.

The above expression for  $r_{sp}$  has been integrated over solid angle, assuming Lambertian emission from the surface of the nanopillar. For the 100x magnification objective with numerical aperture 0.7, we have earlier calculated that 9% of the total photoluminescence from a single upright nanopillar is collected since most of the photons are emitted outside the collection cone of the objective [3]. Using this fact and the SEM-measured surface area of the nanopillar, we are able to calculate the photoluminescence intensity  $r_{sp}$  from the total power collected by the objective. The InP nanopillar and QW nanopillar growth samples have pillars with nearly identical diameters. The corresponding growth recipes were similar except for the 5 nm InGaAs layer in the case of the QW sample. Hence, the absorbed power at a given power density is going to be very similar for the InP nanopillar and the QW nanopillar.

In addition, in order to estimate the total collected power from the measured spectrometer counts, we need to estimate the collection efficiency of the setup using a reference sample. We used a 99% reflective Lambertian reference (Spectralon™) illuminated with a 1550 nm laser to measure the collection efficiency. The power behind the objective is measured using a Thorlabs™ S122C calibrated germanium photodiode. In the photoluminescence measurement, the 1550 nm laser is replaced with a 660 nm laser for non-resonant excitation of the quantum wells. In the CW pumping experiment for the undercut laser, a 980 nm laser (see Fig. S1) was used for more uniform pumping of the active region down to the base of the pillar. The PL experiments were performed by

optimizing the position of the nanopillar for maximum PL counts, so as to make sure the nanopillar is at the peak intensity position in the beam. Using the measured collection efficiency from the 99% reflective Lambertian reference and the numerical aperture of the objective, the quantitative photoluminescence intensity  $r_{sp}$  can be determined and hence the chemical potential of the photons  $\mu$ .

To determine the pump intensity in  $W/cm^2$ , the beam distribution is measured using the knife edge technique [4]. For the non-resonant excitation case, the peak intensity for Fermi level split  $\mu = \hbar\omega$  is quoted as the transparency power density. This is a conservative estimate since not all of the incident 660 nm photons are absorbed by the nanopillar cross section.

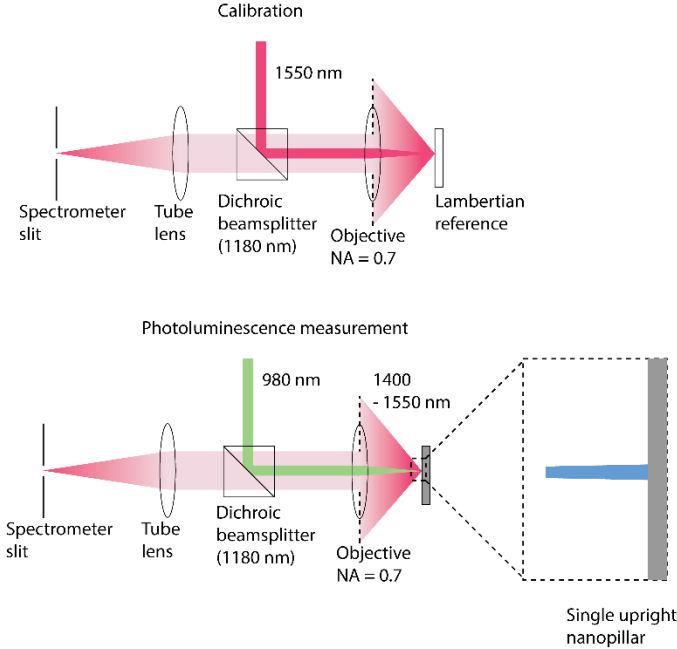


Fig. S1: Setup calibration and Fermi level split measurement – Both excitation and photoluminescence collection were performed using the same 100x objective, with a dichroic beamsplitter to separate the pump and output photons. The calibration was determined using a Lambertian reference illuminated with a 1550 nm laser, in order to emulate the Lambertian emission of the nanopillar. These counts were measured using the spectrometer and OMA-V InGaAs CCD array. The power behind the sample (in the calibration situation) was measured using a photodiode, so the reflected power from the Lambertian could be determined. The photoluminescence experiment for resonant excitation of the quantum wells is shown above. The same was also done with a 660 nm pump for pumping the cladding.

Lastly, we emphasize that although this calibrated photoluminescence technique is widely used for solar cell characterization, the experimental extension to high excitation power near transparency is new. The theory for this is described in section 9 (“Laser radiation”) of Ref. 1. In this work, the reported Fermi level split measurement is for single quantum well nanopillars without a cavity structure (directly on silicon). This is verified by the absence of modes at any pump level. However, modes can be observed at all pump levels for a nanopillar transferred to a low index substrate (as described below). These modes become sharper at higher pump intensity as the modal gain increases, and the modal gain can be estimated using the Hakki-Paoli technique [5].

Further evidence of pumping to transparency is obtained from the shape of the PL spectrum. We have observed a characteristic

blue shift in the PL peak when the quantum well is pumped above transparency. To be precise, the PL peak blue shifts to a higher energy by 60 meV ( $\sim 110$  nm) above the low excitation PL peak energy when pumped up to  $3 \text{ kW/cm}^2$ . This is due to the Fermi inversion factor shifting bluer and into the density of states of the quantum well, thus saturating the emission of the lower energy states. This provides a convenient qualitative confirmation of transparency.

## II. INTERNAL LUMINESCENCE YIELD AND INTERFACE PASSIVATION

The internal luminescence yield (alternately internal quantum efficiency IQE) of three samples (InGaAs quantum well in InP nanopillar, undoped InP nanopillar and planar InGaAs/InAlGaAs planar quantum well epi on InP substrate) was determined using the measured photoluminescence counts. The ratio of room temperature externally collected photons to low temperature external photons is equal to the internal yield in the absence of photon recycling [6]. Photon recycling is negligible in our case since the active region is a thin quantum well. Photon recycling of the band-edge photons is not expected in the InP nanopillar either since the nanopillar diameter is sub- $\mu m$ . The luminescence yield measurement is also based on the assumption that at sufficiently low temperature, the thermally activated non-radiative recombination rate is negligible compared to the radiative rate. The technique has been used ubiquitously for determining the material quality of novel materials [7,8]. Here we used the ratio of 300K PL counts to 5K counts in order to obtain the internal yield. Writing the rate equation for carriers in the active region:

$$\frac{dn}{dt} = G - R = G - (An + Bn^2 + Cn^3) = 0 \text{ (steady state)} \quad \dots(S2)$$

where A, the Shockley-Read-Hall (SRH) recombination coefficient is dominated by interfacial and surface recombination in the case of pristine material such as in the nanopillars. B is the radiative recombination coefficient, C is the Auger coefficient, G is the generation rate in electron-hole pairs/cm<sup>3</sup>/s (proportional to pump), R is the recombination rate and n is the carrier density. The internal yield at room temperature is then  $Bn^2/G$ . Assuming the SRH and Auger processes are frozen out at 5K, we obtain  $G = Bn^2$  ( $T = 5K$ ). Then, the internal yield is simply:

$$\eta_{int} = \frac{Bn^2(300 \text{ K})}{Bn^2(5 \text{ K})} \quad (S3)$$

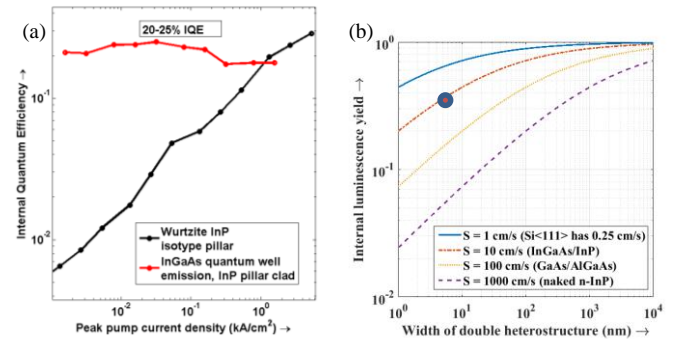


Fig. S2: Internal luminescence yield (or Internal quantum efficiency IQE): (a) the measured internal quantum efficiency as a function of pump power for the InGaAs quantum well presented in Fig. 2(c) of the main manuscript, compared with the IQE of the undoped InP sample. It can be particularly noted that the IQE of the quantum well is much higher than that of the undoped InP sample at low pump power. (b) The maximum theoretical IQE was estimated using a simple A, B, C model

with the non-radiative SRH coefficient  $A$  being dominated by interfacial recombination. This peak IQE was determined as a function of the double heterostructure width and is plotted for various interfacial recombination velocities in the figure. The measured peak IQE (red dot) of  $\sim 25\%$  is consistent with an interfacial recombination velocity of 10 cm/s in a 5 nm InGaAs/InP quantum well heterostructure.

This can then be obtained at each pumping level at both 5K and 300 K. The ratio is plotted in Fig. 2(a) below for the InP pillar as well as InGaAs quantum well in nanopillar emission. Firstly, we observe that the quantum well IQE is insensitive to pump level, and stays at a relatively high value of 20-25% even at low pumping levels below 100 A/cm<sup>2</sup>. Note that the electrical pump current was obtained from the incident optical pump power by converting 100% of the 660 nm incident photons to electrons, and can be considered an equivalent electrical pump current density.

On the other hand, we observe that the undoped InP starts with a low IQE of 0.3% that increases with pump power due to the saturation of non-radiative centers. This reflects the benefit of carrier concentration in the quantum wells. The photons absorbed in the cladding are rapidly captured into the quantum well, where the radiative recombination rate benefits from the carrier concentration.

Here, we elucidate the measured IQE using an A,B,C model for carrier recombination. If  $d$  is the width of the double heterostructure,  $S$  the interface recombination velocity, then the SRH coefficient can be determined from the surface to volume ratio of the active region [9]:  $A = 2S/d$

Then, the IQE at a given carrier concentration  $n$ , under high level excitation ( $n \gg$  background doping) becomes:

$$\eta_{int} = \frac{Bn^2}{An+Bn^2+Cn^3} = \frac{Bn^2}{\frac{2S}{d}n+Bn^2+Cn^3} \leq \frac{B}{B+2\sqrt{\frac{2SC}{d}}} \quad (S4)$$

Essentially, as carrier concentration is increased when the active region is pumped, the radiative recombination rate grows faster than the interfacial recombination, leading to increasing IQE, until the Auger rate starts to increase. There then exists a peak IQE and an optimal carrier concentration (or optimal doping level) for

maximum IQE. This maximum IQE is given by the expression on the right above:  $B/(B + 2\sqrt{AC})$ .

The maximum IQE at the optimal carrier concentration has been plotted on figure 2(b) above, as a function of double heterostructure width, for typical interfacial recombination velocities observed in lattice-matched III/V semiconductor heterostructures, using the radiative and Auger coefficients of In<sub>x</sub>Ga<sub>1-x</sub>As lattice matched with InP [10-13]. The measured peak IQE of 25% is consistent with the expectation for a 5 nm thin quantum well with  $\sim 10$  cm/s interfacial recombination velocity. Lastly, we attribute the lack of pump dependence in the measured IQE in Fig. 2(a) to the presence of background doping in the MOCVD growth, which is highly beneficial since it improves the carrier concentration and enhances radiative rate even at low excitation power levels.

### III. FABRY-PEROT MODES IN TRANSFERRED NANOPILLAR LASERS

To enhance optical feedback, as-grown InP nanopillars with five InGaAs quantum wells were transferred to sapphire substrate by mechanical wiping. In the lying-down nanopillar, semiconductor-air interfaces at both top and bottom of nanopillar provide strong reflections, forming a horizontal high quality factor Fabry-Pérot cavity. This is the typical configuration for studying nanowire lasing behavior, and we have characterized this for completion and consistency with the body of work on short-wavelength lasers. The structure has been illustrated in the inset of Fig. 3(a).

Lasing at the wavelength of 1300nm is achieved using an optical pump (femtosecond titanium:Sapphire pulses at a wavelength of 900 nm) at 5 K. Fig. 3(a) shows the PL spectra below and above lasing threshold. Under low pump power (blue curve in Fig. 3(a)), Fabry-Pérot modes are clearly observed, with a distinctive feature that optical mode wavelengths are equally spaced. The mode spacing  $\Delta\lambda$  is measured to be 17nm, matching the theoretical value determined by:

$$\Delta\lambda = \frac{\lambda^2}{2n_g L} \quad (S5)$$

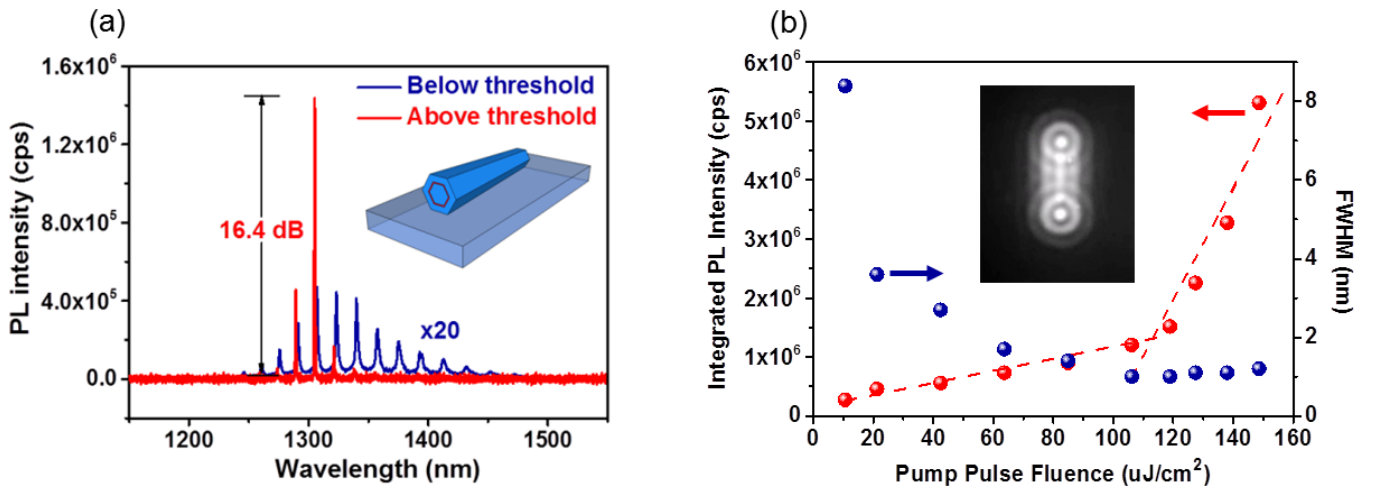


Fig. S3: Transferred nanopillar laser: (a) Photoluminescence (PL) spectra of a transferred nanopillar below and above lasing threshold. The emission below threshold is multiplied 20 times for visibility. The inset is a schematic of a transferred nanopillar on a sapphire substrate. The PL experiment was conducted at a temperature of 5K and under 900nm pulsed pump laser (b) PL intensity and full width-at-half-maximum (FWHM) of the lasing mode at  $\sim 1.3\mu\text{m}$  as a function of pump pulse fluence. The inset is the near field image of the nanopillar emission above lasing threshold.

where  $n_g$  is the group index ( $\sim 4.2$ ) and  $L$  is cavity length ( $12 \mu\text{m}$ ). When the pump power exceeds lasing threshold, one of the Fabry-Pérot modes at the wavelength of  $\sim 1300\text{nm}$  dominates the spectra with a side mode suppression ratio of 16.4 dB.

Several other characteristics confirm the lasing behavior. First, as shown in the red trace in Fig. 3(b), PL emission intensity plot as a function of pump pulse fluence exhibits a non-linear kink, highlighting the lasing threshold of this transferred nanopillar. Additionally, the blue trace of Fig. 3(b) shows that full-width-at-half-maximum (FWHM) of the lasing mode at  $\sim 1.3\mu\text{m}$  narrows to  $\sim 1\text{nm}$  around the lasing threshold. Finally, a near-field image above lasing threshold (the inset of Fig. 3(b)) shows the interference pattern between the top and bottom end facet emission from the nanopillar, confirming the spatial coherence of light.

We have also measured regularly spaced Fabry-Pérot modes in the nanopillar lasers grown on SOI (Fig. 3(b) in the main manuscript). The mode spacing for these lasers was 9 nm and 11

nm respectively, corresponding to an effective cavity length of  $22.7 \mu\text{m}$  and  $18.5 \mu\text{m}$  respectively. A long laser cavity helps to build up sufficient round trip gain to reach lasing threshold, in spite of the thin quantum well active region.

#### IV. THERMAL RESISTANCE OF NANOPILLAR STRUCTURE

In order to address the thermal performance of a nanopillar/nanowire based laser structure, we fabricated a simple n-doped InP nanopillar resistor. The goal is to measure the thermal dissipation of the nanopillar structure. The single nanopillar resistor is electrically biased at a certain current and voltage, while simultaneously being illuminated at low excitation intensity with a 660 nm pump laser. The photoluminescence (PL) counts are recorded. This is repeated as a function of current bias, in order to determine the PL peak shift as the bias is increased. From the

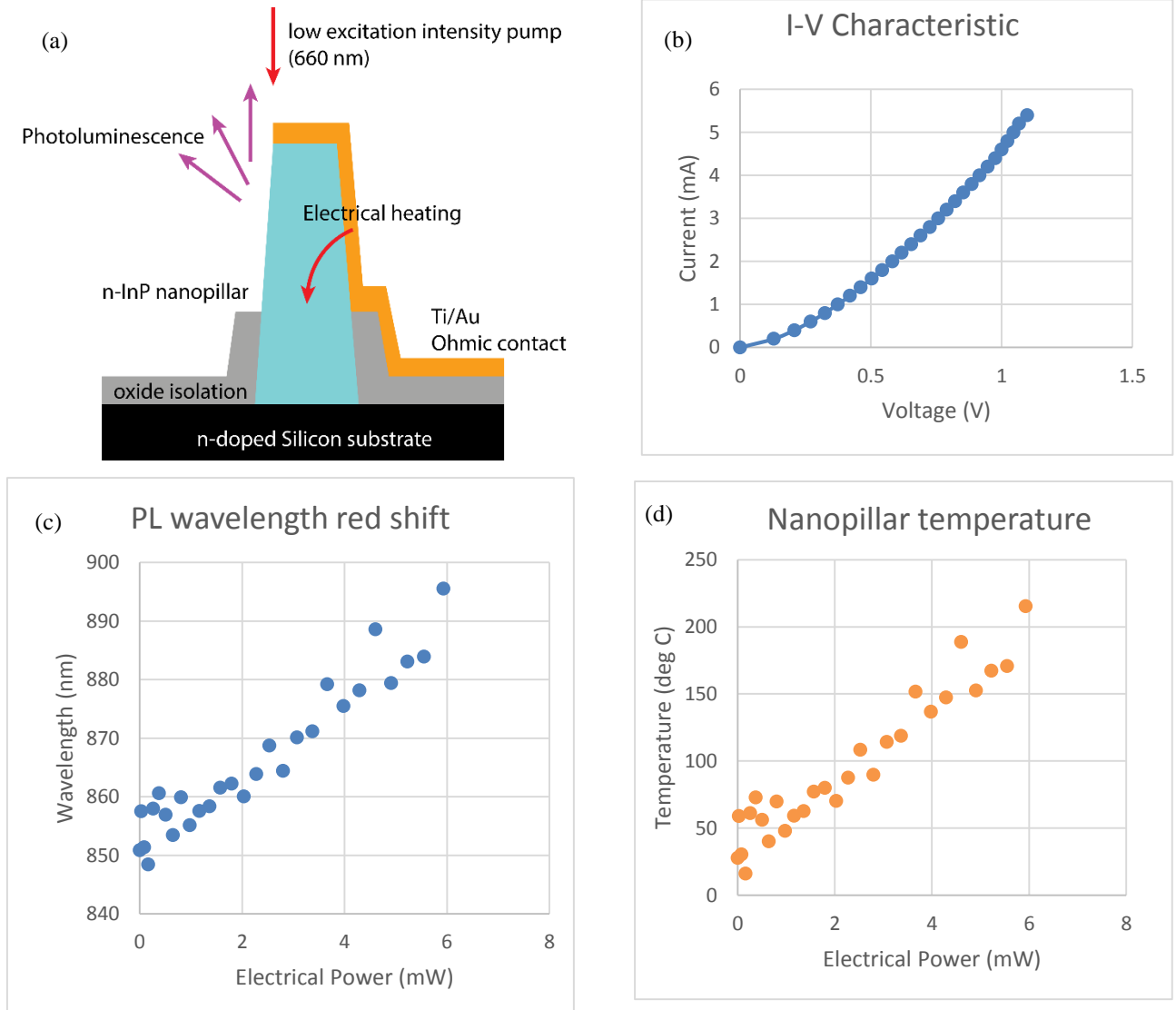


Fig. S4: Nanopillar thermal resistance: (a) Schematic of the fabricated device, with fabrication details in Ref. 14 (b) I-V characteristic of the single nanopillar resistor, showing close to Ohmic characteristics, (c) PL wavelength red shift as a function of electrical power dissipation – the starting wavelength is blue shifted compared to the Wurtzite band edge of 875 nm due to the doping induced Burstein-Moss shift, (d) Inferred nanopillar temperature from the Varshney coefficient for InP.



Varshni coefficient of InP, the temperature of the nanopillar can then be determined.

This allows us to determine the temperature at different dissipation powers in the nanopillar resistor structure – allowing the thermal resistance in K/mW to be measured. This is an important metric, since it allows us to determine the rise in the active region temperature as the laser is pumped harder. Ideally, a low thermal resistance is good for device performance. However, due to the high surface to volume ratio and geometry of the pillar, the measured thermal resistance is rather high at  $\sim 33$  K/mW (see fig. 4). Due to the poor thermal dissipation, under typical laser bias conditions, we will expect to have the nanopillar active region be  $\sim 50$  K above the substrate temperature.

In this case, it becomes all the more important to develop a thermally robust active region. In the undercut laser, we have performed temperature dependent characterization and determined that the characteristic temperature of the lasing threshold is 128 K (with respect to the substrate temperature). This attests to the robust thermal performance of the active region, in spite of the high thermal resistance.

## V. QUANTUM SIZE EFFECT AND $\text{In}_x\text{Ga}_{1-x}\text{As}$ ALLOY CONCENTRATION

The quantum well width variation was used to verify the quantum size effect as shown in figure 2(d) in the main manuscript. Further analysis has been performed to fit the Indium concentration of the quantum well alloy to the width variation. The Zinc Blende phase material parameters (bandgaps, band offsets, Varshni coefficients, bowing parameters and effective masses) were obtained from [15, 16]. These were used to solve for the quantum well ground state energy (interband transition) and the result has been plotted as a function of the width in Fig. S5. The data for  $x = 0.45$  shows reasonable agreement with the experimental data. We can expect to have better accuracy once all the relevant parameters for the Wurtzite phase have been measured. Note that the lattice constant for  $\text{In}_{0.45}\text{Ga}_{0.55}\text{As}$  is  $5.836\text{\AA}$ , which is 0.55% mismatched to the InP core at  $5.869\text{\AA}$ . The corresponding critical thickness for planar epitaxial growth is about 10 nm [17]. However, we have been able to grow 5 quantum wells embedded within the InP nanopillar. This corresponds to 25-30 nm total InGaAs thickness, which is 2-3x above what would be possible with planar epitaxy.

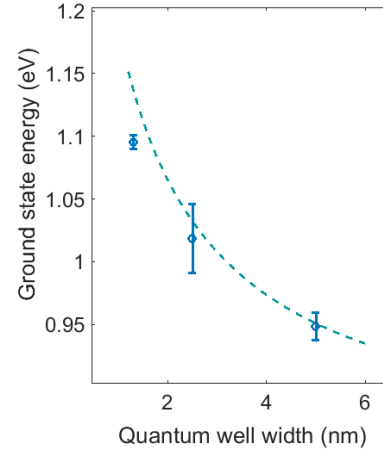


Fig. S5: Plot of the QW ground state energy vs. QW width for the case of a single  $\text{In}_{0.45}\text{Ga}_{0.55}\text{As}$  QW embedded in InP. The QW with finite barrier was numerically solved from reported material parameters. The measured bandgaps are also plotted as a function of quantum well width (corresponding to Fig. 2(c) in the main manuscript), with good agreement between model (dashed line) and measurement (points) observed.

## V. References

1. P. Wuerfel, "The chemical potential of radiation," J. Phys. C: Solid State Phys. **15**, 3967-3985 (1982).
2. H. Fang, H. A. Bechtel, E. Plis, M. C. Martin, S. Krishna, E. Yablonovitch, and A. Javey, "Quantum of optical absorption in two-dimensional semiconductors," Proc. Natl. Acad. Sci. U.S.A. **110**, 11688-11691 (2013).
3. T.-T.D. Tran, H. Sun, K. W. Ng, F. Ren, K. Li, F. Lu, E. Yablonovitch, and C. J. Chang-Hasnain, "High Brightness InP Micropillars Grown on Silicon with Fermi Level Splitting Larger than 1 eV," Nano Lett. **14**, 3235-3240 (2014).
4. J. M. Khosrofi, and B. A. Garetz, "Measurement of a Gaussian laser beam diameter through the direct inversion of knife-edge data," Appl. Opt. **22**, 3406-3410 (1983).
5. B. W. Hakki, and T. T. Paoli, "Gain spectra in GaAs double-heterostructure injection lasers," J. Appl. Phys. **46**, 1299-1306 (1974).
6. I. Schnitzer, E. Yablonovitch, C. Caneau, and T. J. Gmitter, "Ultrahigh spontaneous emission quantum efficiency, 99.7% internally and 72% externally, from AlGaAs/GaAs/AlGaAs double heterostructures," Appl. Phys. Lett. **62**, 131-133 (1993).
7. S. Watanabe, N. Yamada, M. Nagashima, Y. Ueki, C. Sasaki, Y. Yamada, T. Taguchi, K. Tadatomo, H. Okagawa, and H. Kudo, "Internal quantum efficiency of highly-efficient  $\text{In}_x\text{Ga}_{1-x}\text{N}$ -based near-ultraviolet light-emitting diodes," Appl. Phys. Lett. **83**, 4906-4908 (2003).
8. A. Laubsch, M. Sabathil, G. Bruederl, J. Wagner, M. Strassburg, E. Baur, H. Braun, U. T. Schwartz, A. Lell, S. Lutgen, N. Linder, R. Oberschmid, and B. Hahn, "Measurement of the internal quantum efficiency of InGaN quantum wells," presented at Proc. SPIE 6486, San Jose, 2007.
9. K. Li, K. W. Ng, T.-T. D. Tran, H. Sun, F. Lu, and C. Chang-Hasnain, "Wurtzite-phased InP Micropillars Grown on Silicon with Low Surface Recombination Velocity," Nano Lett. **15**, 7189-7198 (2015).
10. R. J. Nelson, and R. G. Sobers, "Interfacial recombination velocity in GaAlAs/GaAs heterostructures," Appl. Phys. Lett. **32**, 761-763 (1978).
11. E. Yablonovitch, H. M. Cox, and T. J. Gmitter, "Nearly ideal electronic surfaces on naked  $\text{In}_{0.53}\text{Ga}_{0.47}\text{As}$  quantum wells," Appl. Phys. Lett. **52**, 1002-1004 (1988).

12. L. W. Molenkamp, and H. F. J. van't Blik, "Very low interface recombination velocity in (Al,Ga)As heterostructures grown by organometallic vapor-phase epitaxy," J. Appl. Phys. **64**, 4253-4256 (1988).
13. E. Yablonovitch, D. L. Allara, C. C. Chang, T. Gmitter, and T. B. Bright, "Unusually low surface-recombination velocity on silicon and germanium surfaces," Phys. Rev. Lett. **57**, 249-252 (1986).
14. W. S. Ko, T.-T. D. Tran, I. Bhattacharya, K. W. Ng, H. Sun, and C. Chang-Hasnain, "Illumination angle insensitive single indium phosphide tapered nanopillar solar cell," Nano Lett. **15**, 4961-4967 (2015).
15. Physical Properties of semiconductors, NSM archive, Ioffe Institute (url: <http://www.ioffe.ru/SVA/NSM/Semicond/index.html> )
16. V. Palankovski, PhD Dissertation, "Simulation of Heterojunction", 2000 (url: <http://www.iue.tuwien.ac.at/phd/palankovski/diss.html>)
18. H. Temkin, D. G. Gershoni, S. N. G. Chu, J. M. Vandenberg, R. A. Hamm and M. B. Panish, "Critical layer thickness in strained Ga<sub>1-x</sub>In<sub>x</sub>As/InP quantum wells", Appl. Phys. Lett. **55**(16), 1668-1670, 1989.